Supplementary material

1. Experimental methodology

We utilize two model fault configurations, which are (1) bare surface Westerly granite (ground and roughened with #120 silicon carbide grit) and (2) a 2 mm-thick quartz gouge layer (116 µm median grain size) sheared between the granite forcing blocks roughened with #240 abrasive. The sample dimensions and fault orientation result in a nominal fault surface area of 9120 mm^2. We do not know precise pore volumes of either bare surface or gouge-filled samples. From surface profilometer measurements and experience with similar samples, we estimate that wear of the 'bare' surface sample produces an approximately 30 µm thick gouge layer following 1 to 2 mm shearing for an estimated fault volume of ~270 mm^3. Likewise, we do not know porosity of this layer, but assuming 5 to 10% implies pore volume of 15 to 30 mm^3. For the quartz gouge experiment, assuming a nominal compaction of 20%, pore volume is about 700 to 1400 mm^3. In subsequent gouge tests with the F-125 quartz gouge, total compaction was between 14 and 25 percent and median grain size was reduced from 116 µm to approximately 69 µm (by weight).

The sample is sufficiently large to allow the addition of a high-resolution wide-bandwidth pressure transducer to be embedded adjacent and in direct hydraulic communication with the fault zone (Figure 1). The strategy follows unpublished experiments of *Weeks* [1980] in which a pressure transducer was placed in close hydraulic and spatial proximity to a water-saturated fault under controlled loading. The sensor (Kulite model HKM-375 with maximum rated pressure of 70 MPa and >400 kHz resonance) is oriented with its 8.1 mm-diameter active face parallel to the fault ~2 mm below the surface, in an 8.5 mm-diameter machined chamber that represents < 0.6% of the total fault area. The fluid chamber at the transducer face has ~120 mm^3 volume that is somewhat larger than the pore volume of the bare surface fault layer and smaller than the volume of the 2 mm gouge layer. Thus, transient pore pressure response may be delayed and attenuated slightly (especially for the bare surface tests), depending on fault zone hydraulic diffusivity. See Section 2 for additional discussion.

The triaxial test geometry is an axisymmetric configuration in which a jacketed cylindrical sample is placed in a pressure vessel that is pressurized with a fluid (Figure 1c). Then, deviatoric stress is applied by advancing a piston against the sample end at a constant rate. Saturated samples were tested over a range of confining pressures between 30 to 75 MPa at controlled external pore pressures of 5 to 20 MPa, and at loading rates between 0.05 and 10 μm/s. Samples were placed between steel end caps and into a 4.4 mm-wall-thickness polyurethane tube to isolate them from the silicone oil confining fluid. In each test, the sample was placed in the pressure vessel and a constant confining pressure (P_c) was applied. All tests were conducted at constant servo-controlled confining pressure. Therefore, both shear and normal stress, resolved on the 30° inclined fault, varied with fault strength in the ratio $\Delta\tau/\Delta\sigma_n = \tan(60°) \approx 1.73$. Deformation tests of this kind are frequently conducted at constant normal stress. A constant P_c test implies that increasing fault strength will result in increasing normal stress and therefore additional compaction (rise in p). From eq. (1), the resultant rise in σ_n^{eff} will be less than, for example, in a drained sample. The precise influence of constant P_c compared to constant σ_n remains to be determined. Sensitivity of p to variations in axial load for the bare surface sample was tested by applying stress steps and measuring pore pressure response. This was done at loads well below the sliding strength to isolate the elastic response of the fault/transducer system. Pore pressure increase was found to be ~0.078 MPa per 1 MPa increase in shear stress.

The pore pressure system (including the sample) was first evacuated, and then the desired external pore pressure was established using distilled water. Pore fluid reached the fault by diffusing through the lower granite sample half. In some tests, a small diameter hole was bored into the lower sample half to within about 1cm of the fault surface to facilitate the diffusion of water from the sample into the fault zone. (Figure 1C). In most configurations, the diffusivity time constant between the fault zone and the external pore pressure system was over 1 hr, requiring extended wait times to establish an initial internal pore pressure. Following the initial application of confining and pore pressures, the piston was advanced under computer control using a proportional servo-control system. A 0.12 mm thickness greased Teflon shim was placed between the piston and the steel end cap to allow lateral slip of the lower sample half that accommodated shearing on the inclined fault. Confining pressure, axial load, and piston position were recorded continuously at 1 Hz. Piston position, measured outside the pressure vessel with a DCDT displacement sensor, was the feedback position control for axial loading. A separate 100 Hz data logger recorded the output of the piston position DCDT, the internal pressure sensor and an internal axial load cell. This internal load cell is immediately below the lower sample half in the load column, 180 mm from the center of the fault (Figure 1c).

2. Pressure response characteristics of the internal pore pressure transducer

Before the experiment shown in Figure 2, two stress steps were applied to the bare surface sample to determine the response characteristics of the internal pore pressure transducer. The sample was first sheared at 60 MPa constant confining pressure ($\sigma_n^{eff} \approx 89$ MPa) and then shear stress was reduced to 80% of sliding strength (at $\sigma_n^{eff} \approx 81$ MPa). In this way, the elastic response of the system could be measured without complication of sliding on the fault surface. At 80% of sliding strength an abrupt displacement step of 66 μm was applied to the piston, resulting in a 4.0 MPa increase in shear stress and a 0.33 MPa increase in p (Figure S1). After a 256 s hold, shear stress was dropped by 4.4 MPa resulting in a 0.32 MPa drop in p. The overall pore pressure sensitivity to changes in shear stress for the bare surface test is therefore $\Delta p/\Delta\tau$ ~0.078 MPa/MPa. This coefficient includes volume changes in both the fault zone and the fluid chamber surrounding the pressure transducer. A separate test employing a fault without porosity would need to be carried out to isolate the effect of the transducer chamber by itself. As noted in the Experimental Method section, porosity of the bare surface fault is estimated to be ¼ to 1/8 the volume of the pressure transducer chamber, although it is likely to be more compliant. The relative importance of the fault zone versus the transducer chamber cannot be determined at this time. In subsequent experiments, a transducer with a smaller orifice was employed. Referring to Figure 2, the stick slip event had a 16 MPa shear stress drop, implying an expected coseismic drop in p of 1.25 MPa. The observed coseismic drop in p was more than twice this value, implying slip-related coseismic fault dilation. In a similar manner, the slow slip drop in shear stress illustrated in Figures 3c and 3d would imply a stress-driven drop in p of ~0.016 MPa while the measured drop was ten times larger. Again, this implies that the measured variations in p are primarily the result of fault slip processes and not elastic response of the fault/pressure transducer system. For the gouge experiments that have significantly larger fault porosity, the effects of the elastic response of the fault/pressure transducer will be much less.

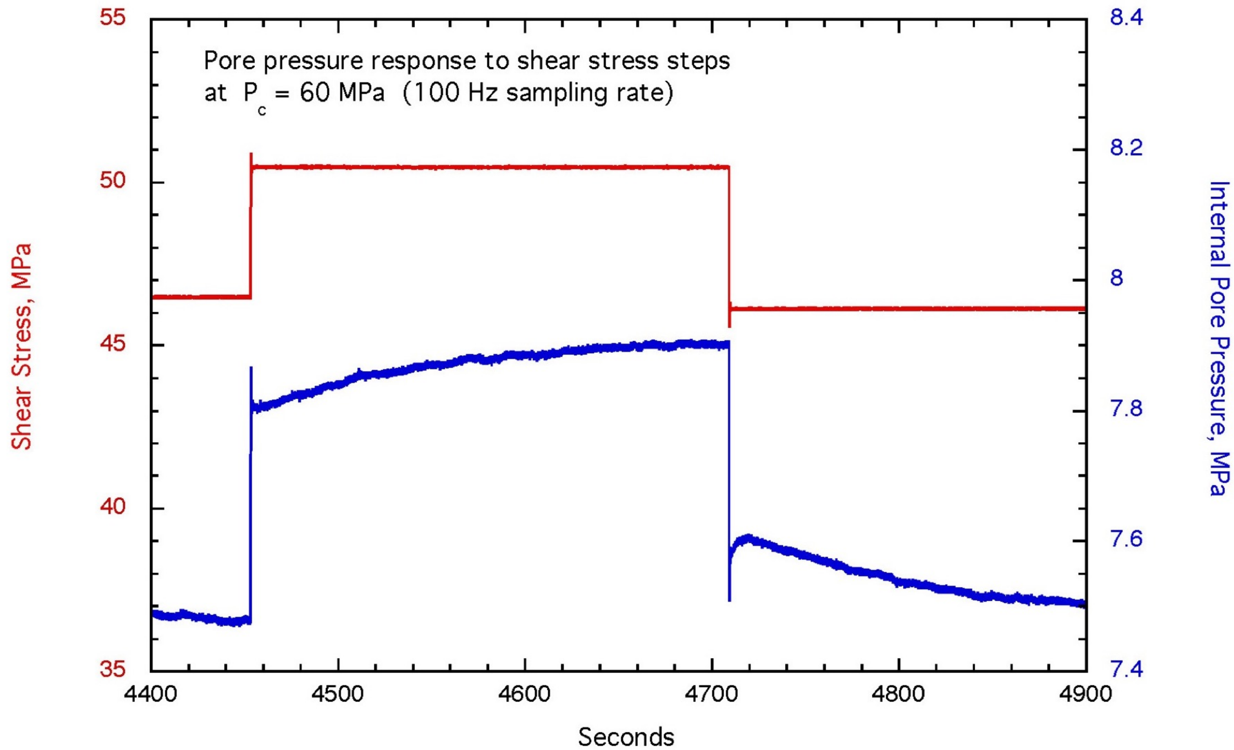

Supplementary Figure 1 – pore pressure response to shear stress steps.

3. Response time of variations in pore pressure

A second question to be addressed in this test is the response time of variations in pore pressure. Data plotted in Figure S1 and expanded in Figure S2 are sampled at 0.01 s intervals. The internal load cell signal used to calculate shear stress has been passed through a preamplifier with a frequency response of ~100 Hz which, at this sampling rate, will show a slight time lag in response to rapid changes. If there are differences in compressibility between the fault surface and the small water-filled chamber surrounding the pore pressure transducer (~120 m^3 volume), there should be a delayed pressure response with a time constant controlled by the fluid diffusivity of the fault surface. This problem has be analyzed for a similar fault geometry with initially bare and finer fault surfaces (compared to this report) in [*Bartlow et al.*, 2012] where a time constant on the order of 10 s was estimated. In that paper, boundary conditions were for flow from an external reservoir at constant pressure. In our case, flow would be to a water-filled chamber adjacent to the fault surface with compressibility near that of water. Consequently, we would expect a shorter diffusion-controlled time constant for the present geometry. This is tested in Figure S3 where the data shown in Figure S2 are plotted as pore pressure versus shear stress. Sampling time, following the step change in the displacement control signal, is annotated on the plot. The maximum unloading rate at 0.2 s is ~60 MPa/s and is determined by the response of the hydraulic servo-control system and the stiffness of the piston and sample column. The slight convex-up curvature between 0 and 0.2 s is probably the frequency response limitation of the axial load preamplifier. Primary unloading in response to the step change in control signal is 0.4 s with no apparent lag in pore pressure response. This implies that the internal pore pressure transducer (factory specification of >400 kHz resonance) is providing reliable pressure data at this 10 ms sampling rate.

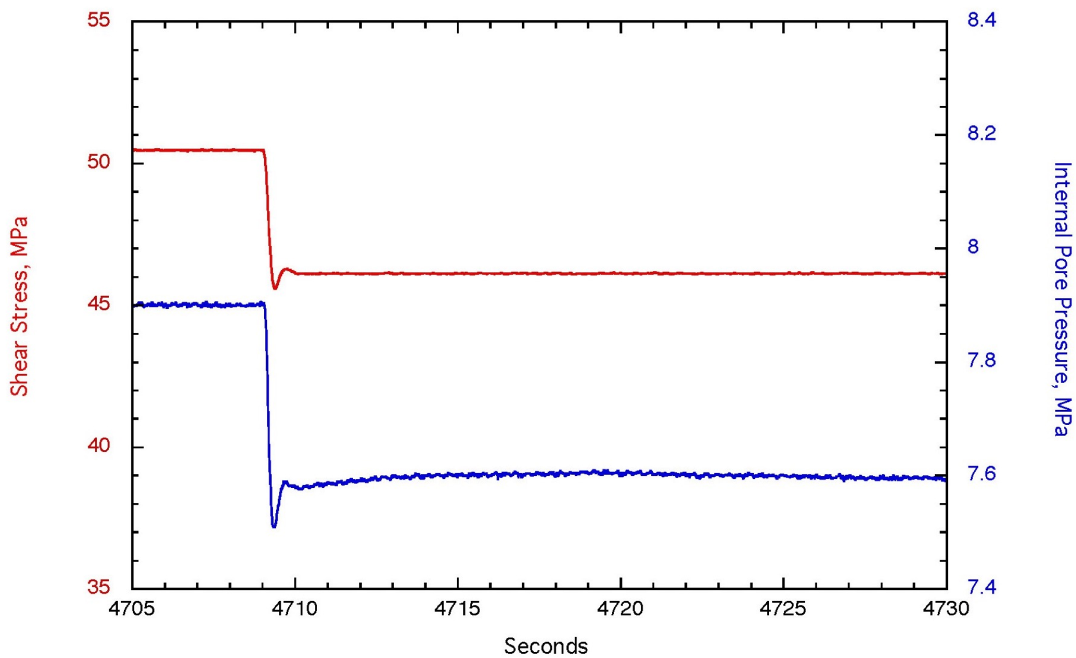

Supplementary Figure 2 – Response time of variations in pore pressure with shear stress

After 0.4 s, the servo-control has under-shot the target stress level and recovers by 0.7 s with a corresponding coincident recovery in p. By 1 s, the servo-control system has settled and all subsequent variations only occur in the pore pressure response. By 10 s, p has recovered by ~0.03 MPa. This may represent the time constant for equilibration of pore pressure in the fault with pore pressure of the transducer chamber. By 50 s, p drifts downwards, possibly recharging microcrack porosity in the granite driving blocks that will tend to open in response to the decrease in axial load. Thus, the main pore pressure response to stress changes, in the absence of fault slip, is elastic and represented by a coefficient of ~0.078 MPa pore pressure per MPa shear stress change. Time dependent response is about ten times smaller with an empirically determined time constant less than 10 s. Again, referring to Figure 2c, the 1.6 MPa rise in *p* following stick slip cannot be the result of elastic volume changes measured that are quantified here. This rise in pore pressure must be the result of either on-fault or off-fault time-dependent compaction.

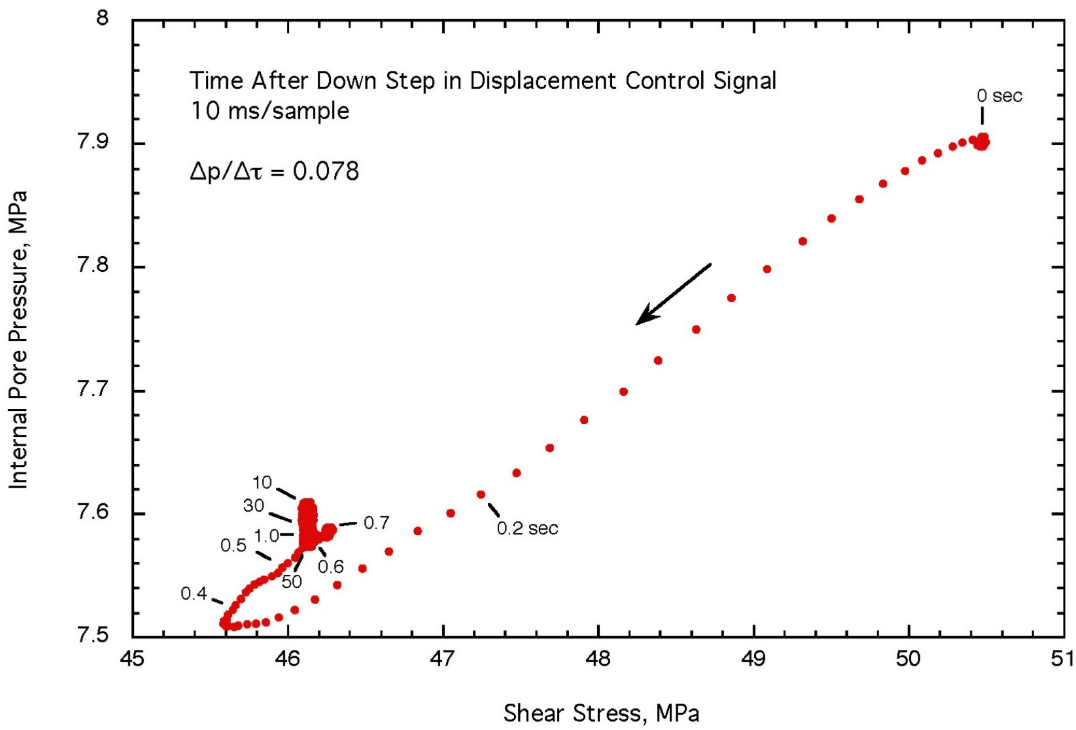

Supplementary Figure 3 – pore pressure vs. shear stress, for data shown in Figure S2.

We end this section by reviewing the short-term pore pressure change prior to the stick slip event in Figure 2a and 2b. Shear stress and internal pore pressure are plotted for the 3 s interval leading up to stick slip in Figure S4. The 0.33 s ripple in both signals is electronic noise. Note that at the scale plotted in Figure 2b, shear stress was steadily increasing until about 10 s prior to failure. In the final 3 s before failure (Figure S4), shear stress drops, even though the rate of piston advance at the load point is constant. This late stage decline in shear stress implies that the fault is creeping faster than the load point velocity of 0.2 μm/s. In the final second before stick slip, a small but measurable increase in weakening rate is observable. The other interesting feature of the shear stress curve is the abrupt loss of strength at the onset of stick slip; occurring within a single 10 ms sampling step.

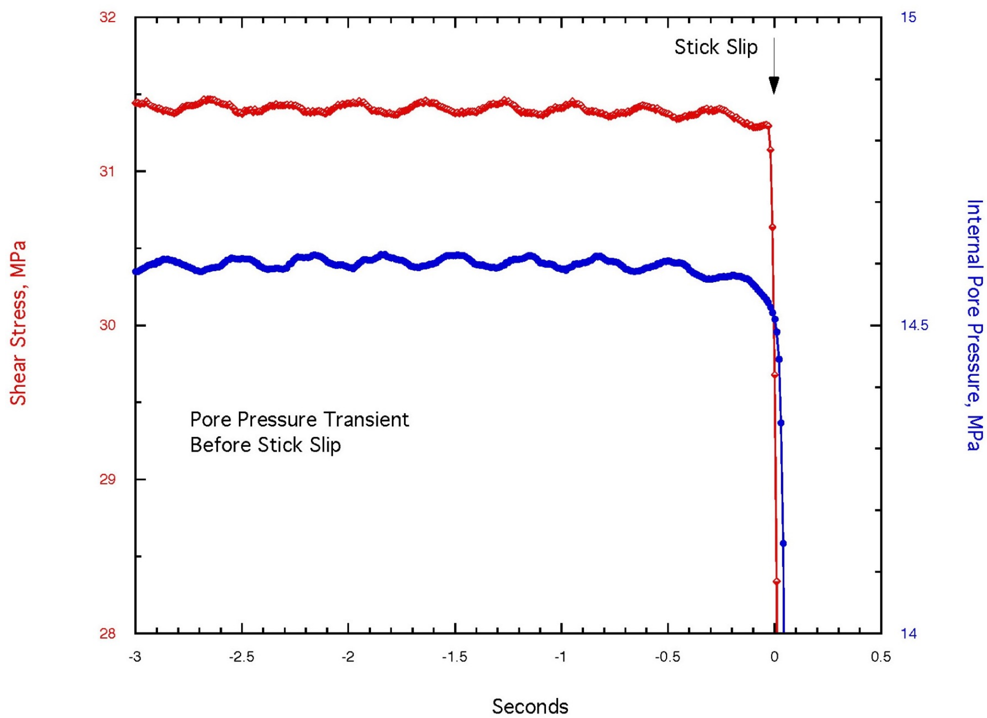

Supplementary Figure 4 - shear stress and internal pore pressure leading up to the stick slip event in figure 2a and 2b.

Internal pore pressure was increasing at an accelerating rate in the minutes before stick slip (Figure 2c). Yet in the final second before failure (Figure S4), *p* decreases at an accelerating rate, implying late stage dilatation in the fault. This drop in pore pressure occurs even though stress is nearly constant in this interval. So the dilatation cannot be an elastic response of the fault/transducer system as measured in Figure S3. We pointed out earlier in this section that the elastic response of the pore pressure system accounts for less than half of the observed coseismic drop in *p*. As shown in Figure S4, there is at most a 50 ms lag in the coseismic response of *p* to the drop in stress, implying that much of the internal pore pressure signal is responding quickly to pressure changes in the fault zone.

4. Frictional heating – 1D shear heating estimates

Following measurements reported in [*Lockner et al.*, 2017], we know that average shear stress and fault slip during rupture were 24 MPa and 0.6 mm, respectively. Then, total work expended during the slip event was approximately 14 kJm^{-2}. High speed recordings of similar dynamic events on this test apparatus suggest a slip duration of about 0.2 ms. Then, a simple 1D heat flow calculation suggests that the peak fault zone temperature rise could exceed 100°C. This presents the possibility that thermal pressurization during the short but energetic slip event might have contributed to dynamic weakening and the relatively large stress drop. This effect will be explored in future experiments.

To estimate shear heating for rapid slip events we use the 1D heat conduction solution of *Cardwell et al.* [1978]for fixed shear zone thickness, *w,* sheared uniformly to a total slip, *D*, at a constant shear resistance, $\hat{\tau}$, over duration, Δt. The temperature change is:

$$\Delta T = \frac{\hat{\tau} D}{2\rho c_p w \Delta t} \int_0^t \left\{ erf\left[\frac{x+(w/2)}{\sqrt{4\kappa(t-t_0)}}\right] - erf\left[\frac{x-(w/2)}{\sqrt{4\kappa(t-t_0)}}\right] \right\} dt_0 \quad 0 < t < \Delta t$$

$$\Delta T = \frac{\hat{\tau} D}{2\rho c_p w \Delta t} \int_0^{\Delta t} \left\{ erf\left[\frac{x+(w/2)}{\sqrt{4\kappa(t-t_0)}}\right] - erf\left[\frac{x-(w/2)}{\sqrt{4\kappa(t-t_0)}}\right] \right\} dt_0 \quad t > \Delta t$$

where ρ is density, c_p is heat capacity, κ is thermal diffusivity, *t* is time, *x* is distance from the center of the fault. The integrals are evaluated numerically.

For the calculations, the coseismic slip, $D = 0.6 \times 10^{-3}$ m, the static offset, is the product of the static stress drop / machine stiffness. The event duration, Δt=2 ms, is a typical value for the duration of motion of the axial piston in doppler laser vibrometer records. The average coseismic slip speed then is ~ 3 m/s. Shear zone thickness, $w = 30 \times 10^{-6}$ m, is inferred from the recovered shear zone and the co-seismic shear stress is $\hat{\tau} =$ 24 x 10^6 Pa. The density, heat capacity and thermal diffusivity assumed in the calculations are ρ= 2800 kg/m^3, c_p=1000 J/kg °K, and κ=1.2 $x10^{-6}$ m^2/s respectively.

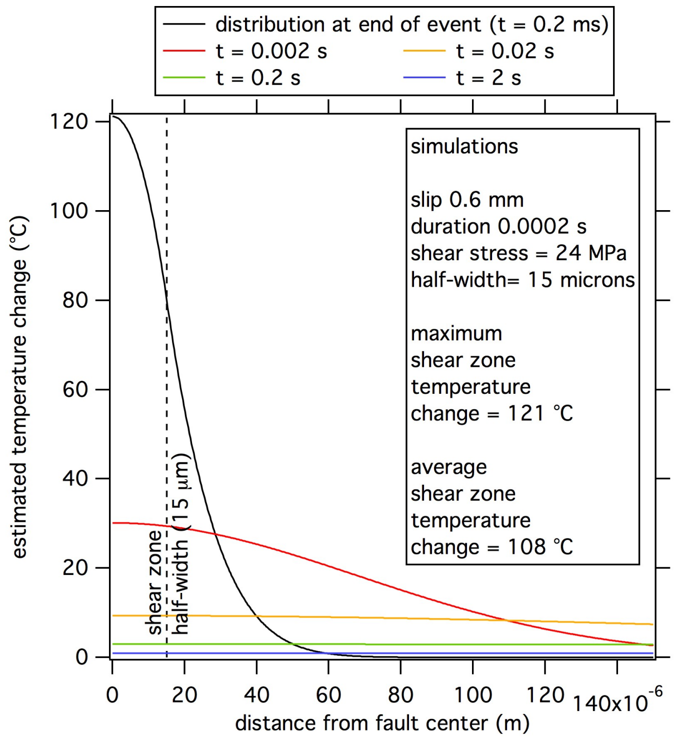

Supplementary Figure 5 – estimated temperature change at different timesteps, as a function of distance from the fault center.

Supplementary Fig. 5 shows the temperature change profiles at the end of the event (*t* =0.2 ms, black) and at order of magnitude increments out to 2 s (blue). At the end of the event the peak temperature change is 121° C, with an average shear zone temperature change of 108° C. By 0.02 s the peak temperature is below 10° C and by 2 seconds is less than 1° C.

References

Bartlow, N. M., D. A. Lockner, and N. M. Beeler (2012), Laboratory triggering of stick-slip events by oscillatory loading in the presence of pore fluid with implications for physics of tectonic tremor, *Journal of Geophysical Research-Solid Earth*, *117*, doi:Artn B11411
10.1029/2012jb009452.

Cardwell, R. K., D. S. Chinn, G. F. Moore, and D. L. Turcotte (1978), Frictional Heating on a Fault Zone with Finite Thickness, *Geophysical Journal of the Royal Astronomical Society*, *52*(3), 525-530, doi:DOI 10.1111/j.1365-246X.1978.tb04247.x.

Lockner, D. A., B. D. Kilgore, N. M. Beeler, and D. E. Moore (2017), The Transition From Frictional Sliding to Shear Melting in Laboratory Stick-Slip Experiments, *Geophys Monogr Ser*, *227*, 105-131, doi:Book_Doi 10.1002/9781119156895.

Weeks, J. D. (1980), Some aspects of frictional sliding at high normal stress, PhD dissertation thesis, 171p. pp, Stanford University.